PHYSICAL REVIEW MATERIALS **7**, 124001 (2023)

Defect-induced states, defect-induced phase transition, and excitonic states in bent tungsten disulfide (WS_2) nanoribbons: Density functional vs. many body theory

Santosh Neupane,[1,2] Hong Tang,[1,3] and Adrienn Ruzsinszky[1,3]
[1]*Department of Physics, Temple University, Philadelphia, Pennsylvania 19122, USA*
[2]*Alvernia University, Reading, Pennsylvania 19607, USA*
[3]*Tulane University, New Orleans, Louisiana 70118, USA*

(Received 22 June 2023; accepted 7 November 2023; published 12 December 2023)

Two-dimensional (2D) transition metal dichalcogenide (TMD) materials have versatile electronic and optical properties. TMD nanoribbons exhibit interesting properties due to reduced dimensionality, quantum confinement, and edge states, which make them suitable for various electronic and optoelectronic applications. In a previous work conducted by our group, we demonstrated that the edge bands evolved with bending can tune the optical properties for various widths of TMD nanoribbons. Defects are commonly present in 2D TMD materials, and can dramatically change the material properties. In this following work, we investigate the interaction between the edge and the defect states in tungsten disulfide (WS_2) nanoribbons with lines of W- or S-atom vacancies defects under different bending conditions, using density functional theory (DFT). To gain understanding about the limits of density functional approximations, we compare results on band gaps and energies of defect states with quasiparticle GW. We reveal interesting semiconductor-metal phase transitions, suggesting potential applications in nanoelectronics or molecular electronics. We also calculate the optical absorption of the bent and defective nanoribbons with the many-body GW-BSE (Bethe-Salpeter equation) approach, revealing a tunable optical spectrum and diverse exciton states in the defective WS_2 nanoribbons.

DOI: 10.1103/PhysRevMaterials.7.124001

I. INTRODUCTION

Condensed matter physics [1–7] has undergone significant advancements since the discovery of single-layer graphene in 2004 [8], with the emergence of a new area of theoretical and experimental study focused on two-dimensional (2D) materials [9–14]. This research has revealed novel physical properties in 2D materials, and has driven the search for new 2D semiconducting materials, leading to breakthroughs in nanoelectronics [15–17], sensing [18,19], energy storage [20,21], energy conversion [22,23], photonics [24,25], optoelectronics [14], magnetoresistance [26], and valleytronics [27,28]. However, like any other materials, defects are inevitable in 2D materials, and their presence can significantly affect their properties [29–32]. Structural defects, such as vacancies, dislocations, and grain boundaries, can alter their electronic and mechanical properties [33–36]. Thus, understanding the role of defects in 2D materials is crucial for optimizing their properties and developing new applications.

Among 2D materials, recent experiments have shown promising breakthroughs in monolayer transition metal dichalcogenides (TMDs) [37–41]. Monolayer tungsten disulfide (WS_2) emits strong photoluminescence (PL) with a high quantum yield [42,43], making it a promising material for 2D optoelectronic devices [14,44,45]. However, the lack of true ohmic contact between the 2D semiconductor and metallic electrodes remains a significant hurdle for device design and fabrication, due to the issue of Schottky contact. Recent research has proposed the use of heterophase homojunctions, which involve coexisting semiconducting and metallic phases built from the same 2D layered materials, as a solution to this problem. Such homojunctions have been shown to enable nearly perfect ohmic connections between semiconducting 2D layers and electrodes by introducing conducting phase patches or regions through locally induced defects and/or strains via laser beam [46] or ion beam [47] irradiations.

Moreover, recent studies have highlighted the crucial role played by defects in the exciton dynamics of monolayer TMDs. Zhou *et al.* [48] and Attaccalite *et al.* [49] have demonstrated the intricate interplay between defects, electronic structure, and optical properties in TMDs. Their findings have provided novel insights into the mechanisms governing exciton generation, recombination, and transport in TMDs. They have shown that defects can significantly affect the exciton lifetime, the radiative and nonradiative decay rates, and the exciton diffusion length in TMDs. These results have important implications for the development of TMD-based optoelectronic devices and suggest new avenues for future research in this field.

Nanoribbons, which are quasi-1D structures with more spatial confinement effects and rich edge states than their 2D counterparts, offer promising potential for designing nanoscale devices [50–52]. By applying uniaxial strains or bending, one can create local strains on the nanoribbons and effectively modify the edge states and band structures, leading to controllable electronic and optical properties [53,54]. In our previous work [55], we have found that the incorporation of bending and doping in WS_2, WSe_2, and WTe_2 nanoribbons can lead to enhanced spin-orbit coupling (SOC) effects and controlled magnetism. This results in spatially varying spin polarization, which has a significant impact on the spin configuration of exciton states.

The focus of this work is twofold: (1) investigating the potential of armchair WS_2 nanoribbons with line defects under different bending radii as a means to realize the semiconductor-metal phase connection in WS_2 homojunctions, (2) understanding the optical response of bent nanoribbons with defects. Meanwhile we are assessing advanced density functional approximations for the electronic structure including defect states.

We examine the correlation between defect and edge states for armchair WS_2 nanoribbons with defects under various bending curvatures using the Perdew-Burke-Ernzerhof (PBE) [56], r^2SCAN meta-generalized gradient approximation (GGA) [57], the modified TASK (mTASK) [58] functional approximations, the higher-level screened hybrid functional HSE06 [59] and the GW method [60–63]. We also investigate optical absorption and excitonic states using the many-body perturbation GW and Bethe-Salpeter equation (BSE) methods. We confirm that the appropriate choice of the defect sites can induce magnetic properties on the WS_2 nanoribbons. Our findings suggest that defects in WS_2 nanoribbons are crucial for inducing magnetic properties. Specifically, we have observed that the appropriate choice of defect sites can result in net magnetization. In contrast, our previous work showed that net magnetization could be achieved only with electron or hole doping in pristine WS_2 nanoribbons [55]. Therefore, we conclude that defects play a significant role in the magnetic behavior of WS_2 nanoribbons. Our results show that a semiconductor-metal phase transition in WS_2 nanoribbons can be driven by line defects under various bending curvatures with the appropriate choice of the defect site. These results broaden the device design strategies for WS_2 homojunctions, and have potential applications in phase-change electrical devices. Our work demonstrates that the optical absorption in A13WS_2 nanoribbons is robust against central sulfur defects, while the spatial extension of excitons can be controlled through bending. Furthermore, intrinsic exciton lifetimes can be modified and controlled through defect introduction and bending, which has important implications for exciton-based quantum controls and probing exciton dynamics.

II. COMPUTATIONAL DETAILS

Density functional theory (DFT) [64,65] calculations were performed using the Vienna Ab initio Software Package (VASP)[66] with projector augmented-wave pseudopotentials [67,68]. In order to avoid the interactions between the nanoribbon and its periodic images, a vacuum layer of more than 12 Å is added between the plane of the nanoribbons and its periodic image. The energy cutoff is 580 eV. The k-point mesh of 1 × 1 × 24 was used for all nanoribbons. The pre-relaxed WS_2 monolayer, which was relaxed with the PBE functional [56], with the in-plane lattice constants of $a = b = 3.321$ Å was used to build the nanoribbons. Then a full structural relaxation for all the nanoribbons was done with PBE with all forces less than 0.01 eV/Å. During the relaxation, the supercell vectors a and b along the x and y axes (corresponding to the ribbon's width and thickness directions, respectively) were kept fixed, while vector c along the z axis (representing the ribbon's periodic or length direction) was allowed to relax. We first create a nanoribbon from a flat monolayer. Then, we employ mechanical bending to achieve the desired curvature in the nanoribbon. We identify the index numbers of the outermost metal atoms using visualization software and subsequently fix them during the geometric relaxation along the x and y directions, unlike all other atoms which are allowed to relax along all three directions.

The G_0W_0 [60–63] and G_0W_0+BSE [69–73] calculations were carried out using BerkeleyGW code [74] by pairing with Quantum ESPRESSO [75]. The wave-function energy cutoff is 70 Ry (≈ 950 eV). The energy cutoff for the epsilon matrix is 18 Ry (≈ 240 eV). The k-point mesh of 1 × 1 × 42 and both valence and conduction bands of 8 were set for optical absorption calculations. The band number for summation is 1100. The correction of the exact static remainder and the wire Coulomb truncation for 1D systems were also used.

WS_2 nanoribbons with W vacancy are usually metallic, where excitonic effects are usually less obvious since the screening effect is stronger in metallic phase. The computational cost of GW for metallic states is much larger since a much finer k grid is needed. We restrict our GW (and BSE) calculations for semiconducting nanoribbons in this study.

The excitonic radiative lifetimes were calculated using Fermi's golden rule based on *ab-initio* BSE technique, described in Spataru *et al.* [76]. The method was initially used for 1D carbon nanotubes, however, was also used for the 2D nanosheet [77].

The SOC was included in all calculations.

III. RESULTS AND DISCUSSIONS

A. Defect-induced phase transition

The nanoribbon with armchair edges is cut from a WS_2 monolayer of the 2H phase, in which the tungsten (W) and chalcogen sulfur (S) atoms form a trigonal prism, as illustrated in Figs. 1(a)–1(c). The edge atoms are passivated with hydrogen (H) atoms. The vacuum layer is added along the direction of the nanoribbon width (x axis) and inserted along the direction perpendicular to the 2D surface of the nanoribbon. The ribbon's thickness direction is along the y axis and periodic (length) direction is along the z axis. The supercell vectors a, b, and c are aligned with the x, y, and z axes, respectively. As illustrated in Fig. 1(a), we employ AnWS_2 to refer to the WS_2 nanoribbons, where n denotes the number of W atoms in the supercell, and n=13 indicates 13 W atoms of the nanoribbon without defects in the supercell. Figures 1(b) and 1(c) depict the relaxed structures of A13WS_2 with W and S defects under various bending curvature radii R, respectively. The calculated band structures of the flat and bent A13WS_2 nanoribbons without defects and with S and W defects using PBE functional [56] are shown in Figs. 2(a)–2(i). Here, the S defect in the nanoribbon refers to the A13WS_2 nanoribbon with a line of sulfur vacancies that is created by removing the central S atom in the lower S atom layer in the supercell and hence forming a S vacancy line parallel to the nanoribbon's length direction. The W defect refers to the line of tungsten vacancies that is created in a similar manner as sulfur vacancies.

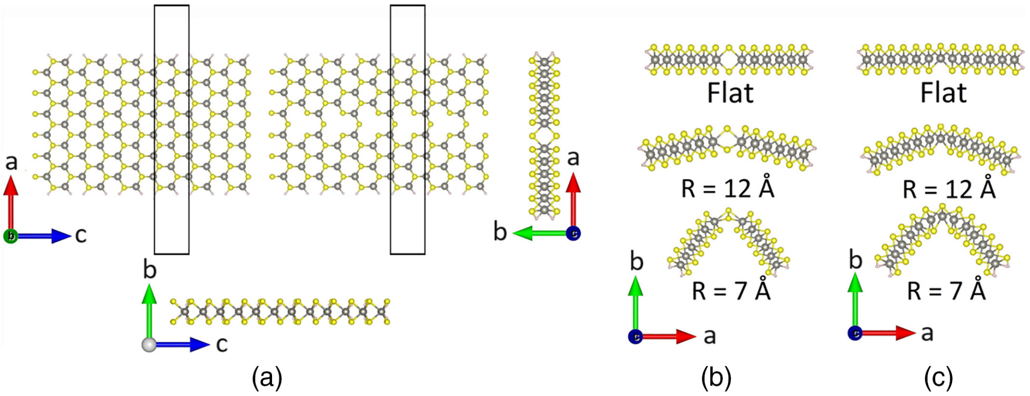

FIG. 1. The structures of the armchair WS_2 nanoribbons and their relaxed structures with S defect and W defect under different bending curvature radii R. The flat nanoribbon $AnWS_2$ with n=13 is shown in (a). n in $AnWS_2$ represents the number of W atoms in the pristine nanoribbon in the periodic supercell, whose unit vectors a, b, and c are aligned with axes x, y, and z, respectively. Gray balls represent W atoms, yellow balls are for S atoms and small white balls are H atoms. The side views of the $A13WS_2$ nanoribbon are also shown in (a). (b) and (c) show the relaxed structures of the $A13WS_2$ nanoribbon under flat, R = 12 Å, and R = 7 Å with W defect and S defect, respectively.

The fundamental band gap of the WS_2 nanoribbon is indirect or direct, depending on the density functional approximation or the choice of bending curvatures and defects in the nanoribbons. By definition it is the difference between the valence band maximum (VBM) and conduction band minimum (CBM) (Table I). The edge-band gap (EG), specific to nanoribbons as quasi-one-dimensional systems, is defined as the difference between CBM and VBM of these localized

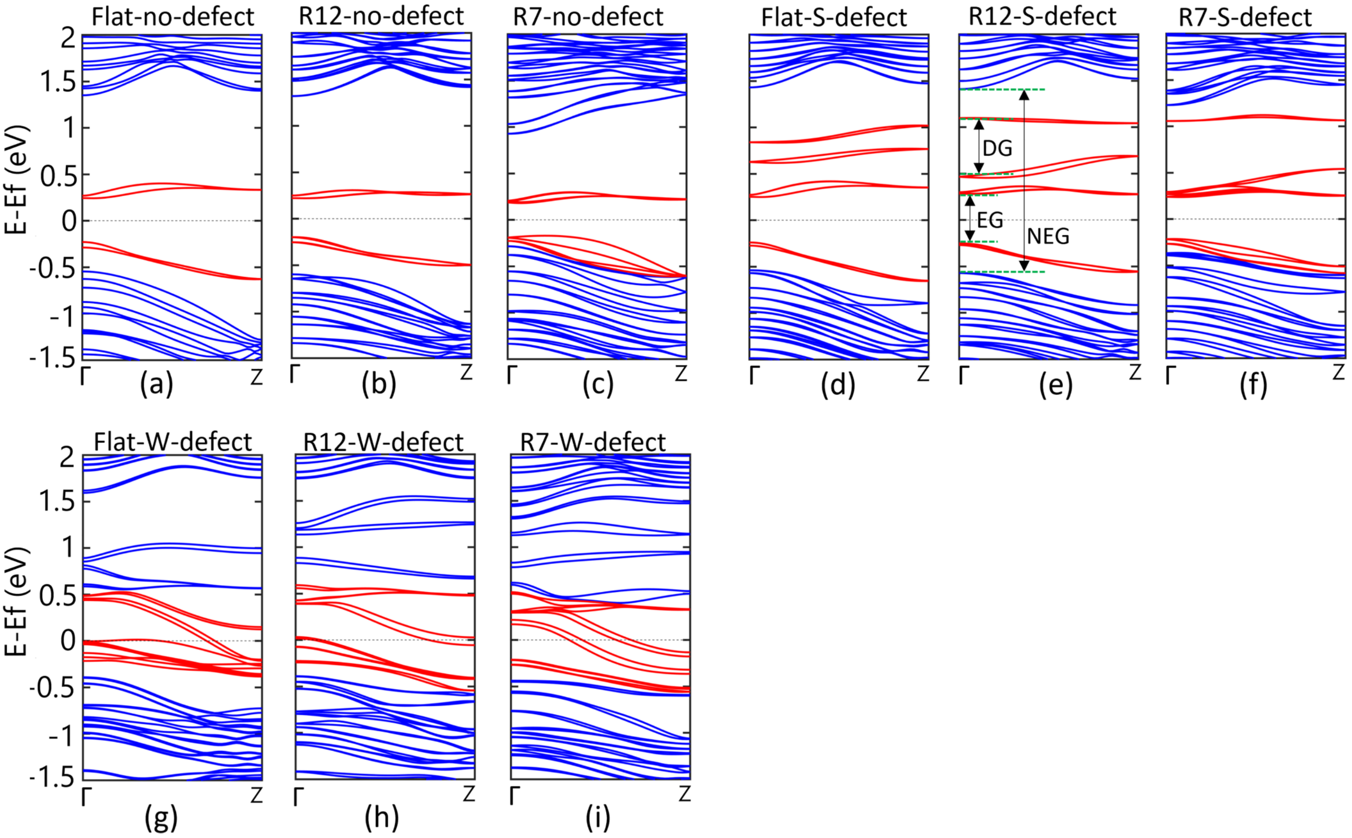

FIG. 2. The band structures of $A13WS_2$ nanoribbons without defect, S defect and W defect under different bending curvature radii R. (a), (b), and (c) are the calculated band structures of the $A13WS_2$ nanoribbons without defects for various bending curvature radii of $R = \infty$ (flat), R = 12 Å and R = 7 Å, respectively. (d), (e), and (f) are the calculated band structures of the $A13WS_2$ nanoribbons with S defect for various bending curvature radii of $R = \infty$ (flat), R = 12 Å and R = 7 Å, respectively. (g), (h), and (i) are the calculated band structures of the $A13WS_2$ nanoribbons with W defect for various bending curvature radii of $R = \infty$ (flat), R = 12 Å and R = 7 Å, respectively. The edge bands around the Fermi level and defect bands above the upper edge bands are shown in red and other bands are in blue.

TABLE I. Comparison of the actual band gaps between VBM and CBM using PBE, r^{2}SCAN, and mTASK density functionals with the higher-level hybrid functional HSE06 or with the G0W0 approximation within many-body perturbation theory for bent and defective A13WS$_2$ nanoribbons.

Bending	Defect	PBE (eV)	r^{2}SCAN (eV)	mTASK (eV)	HSE06 (eV)	GW (eV)
R = ∞ (flat)	None	0.47 (indirect)	0.73 (direct)	1.00 (direct)	1.25 (direct)	1.82 (direct)
	S	0.49 (indirect)	0.75 (direct)	1.08 (direct)	1.27 (direct)	1.83 (direct)
R = 12 Å	None	0.42 (indirect)	0.67 (direct)	0.84 (direct)	1.13 (direct)	1.80 (direct)
	S	0.53 (indirect)	0.79 (direct)	0.96 (indirect)	1.28 (direct)	1.95 (direct)
R = 7 Å	None	0.35 (indirect)	0.54 (direct)	0.77 (direct)	1.00 (direct)	1.67 (direct)
	S	0.45 (indirect)	0.53 (indirect)	0.53 (indirect)	1.00 (direct)	1.66 (direct)

in-gap states, while the non-edge-band gap (NEG) is defined as the difference between the bottom of the conduction band continuum and the top of the valence band continuum (VBC), both at the Γ point [Fig. 2(e)]. In addition to the edge bands near the Fermi level as in-gap states, there are four defect-induced bands above the upper edge bands in the conduction band region, clearly seen in the Figs. 2(d), 2(e) and 2(f). The defect gap (DG) at Γ is defined as the difference between the minimum of the upper defect bands at Γ and the maximum of the lower defect bands at Γ as shown in Fig. 2(e). Here we report a similar variation in the NEG and EG of the pristine A13WS$_2$ nanoribbons with bending curvature as discussed recently by Tang *et al.* [55] for A13WSe$_2$. In case of S defect, the conduction defect bands move close to the edge bands with increasing bending curvatures. For the largest bending curvature $\kappa = 0.142/\text{Å}(R = 7\ \text{Å})$, the lower defect bands merge into the upper edge bands. We find a semiconducting behavior in the pristine and S-defective A13WS$_2$ nanoribbons with various bending radii. In contrast, the A13WS$_2$ nanoribbons with central W vacancy exhibit metallic nature. Inspired by the potential of defects in semiconductor-metal phase change in A13WS$_2$ nanoribbons, we have extented our study to relatively smaller and larger sized (A7WS$_2$ and A25WS$_2$) nanoribbons with different bending curvatures. We show that a very controlled semiconductor-metal phase transition can be achieved in AnWS$_2$ (n = 7, 13, 25) nanoribbons with the combination of bending and defects as displayed in Fig. 3. This can be proposed as an alternative way to realize a heterophase homojunction that shows ohmic contact in TMDs transistors via laser irradiation [46]. The homojunction may be realized by a design in which the contact area is designed as a bent portion of the nanoribbon. The bent portion of the nanoribbon can be grown (or clamped) on a curved surface of a conducting substrate. The highly strained region between the flat and bent regions can be mitigated by allowing a relatively long distance of transition from the flat and bent regions. The possible localized states can be reduced. This finding in WS$_2$ nanoribbons has the potential to impact various fields and create new opportunities for technological advancement.

The density of states (DOS) analysis for A13WS$_2$ without defect, with S and W defects is shown in the top, middle, and bottom panels of Fig. 4, respectively. The total four W atoms located at the edges, two W atoms at each edge, are counted as the edge W atoms. The three W atoms near the position of the S defect and four W atoms near the position of W defect of the nanoribbon are counted as the near defect W atoms, as shown in Supplemental Fig. S1 [78]. In the pristine nanoribbons, the edge W atoms dominate the DOS around the Fermi level, as shown in the top panels of Fig. 4, and the edge bands show up in the range of 0–0.5 and -0.5–0 eV, the W atoms close to the midribbon area contribute more to the top of the valence band (approximately -0.5 to 0 eV) with increasing bending curvature.

In the nanoribbons with S defect, the edge W atoms again dominate the DOS around the Fermi level, as shown in the middle panels of Fig. 4. In the flat nanoribbon, the near defect W atoms dominate the DOS at about 0.5 to 1 eV from the conduction bands. Those bands corresponding to the DOS at about -0.5 to -1 eV is contributed by all W atoms.

In the nanoribbons with a W defect, the DOS analysis shows that the bands crossing the Fermi level mainly consist of the edge W atoms and near defect W atoms in flat and bent (R = 12 Å) nanoribbons, while mainly contributed by near

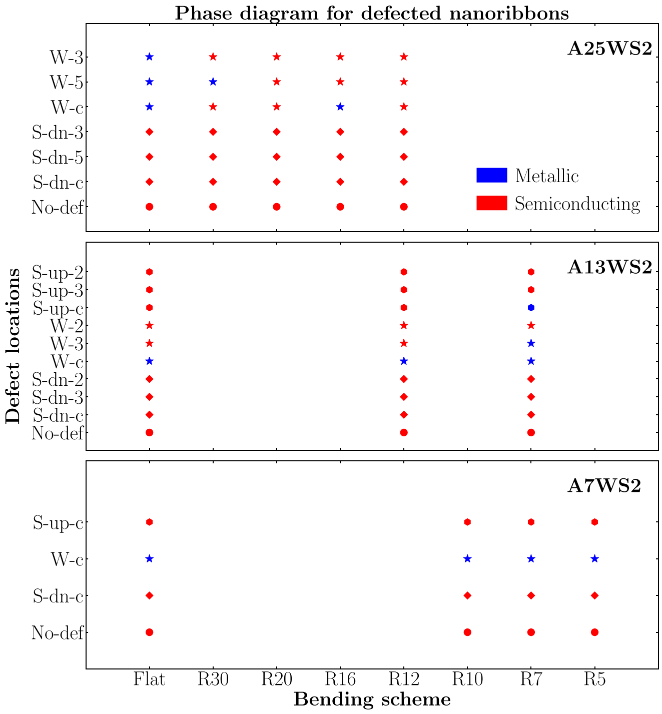

FIG. 3. The phase diagram for different sizes of WS$_2$ nanoribbon with various bending radii. The defect locations labeled in the y axis for different sizes of the nanoribbons are shown in the Supplemental Fig. S2 [78]. No-def in y axis refers to the nanoribbons without defects.

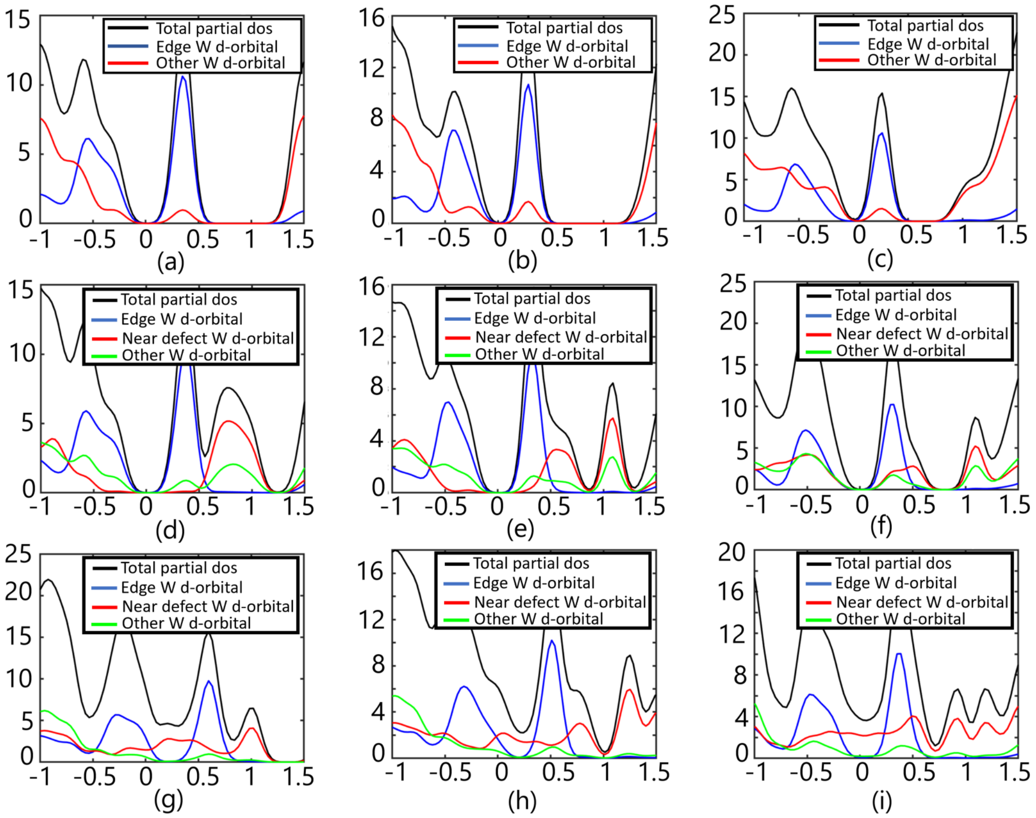

FIG. 4. (a), (b), and (c) represent the analysis of the density of states of A13WS$_2$ nanoribbon without defect under different bending radii. (d), (e), and (f) represent the analysis of the density of states of A13WS$_2$ nanoribbon with S defect under different bending radii. See the title on each plot for the bending radius. (g), (h), and (i) represent the analysis of the density of states of A13WS$_2$ nanoribbon with W defect under different bending radii. Right, middle, and left correspond to the flat, R = 12Å and R = 7Å nanoribbons, respectively. Green, red, blue, and black curves represent the contributions from other W d orbital, near defect W d orbital, edge W W d orbital and total partial density of states, respectively. They are calculated with PBE and the SOC effect included.

defect W atoms in bent (R = 7 Å) nanoribbon, as shown in the bottom panels of Fig. 4.

In our previous work, we demonstrate that only doping induces net magnetization. Doping makes our nanoribbons electrically charged, but the nanoribbons still remain electrically neutral with S or W line defects. Doping can introduce magnetic impurities into the material, which can lead to the formation of local magnetic moments and induce net magnetization. For example, doping a TMDs nanoribbon with transition metal impurities can introduce local magnetic moments that contribute to the overall magnetization of the material. Defects, on the other hand, can induce net magnetization through the modification of the electronic structure of the material. For example, defects can introduce localized states within the band gap of the material, which can lead to the formation of magnetic polarons or the localization of magnetic moments in the vicinity of the defects. Such magnetic moments are great testbeds for density functional approximations. We investigate the magnetization of pristine and defective A13WS$_2$ nanoribbons under three different bending curvatures: flat, R = 12 Å, and R = 7 Å. Our results, presented in Table II using the PBE functional, indicate that the pristine and S-defective nanoribbons have either no net magnetization or negligible magnetization. We observe a net magnetization in the nanoribbons in the presence of a W vacancy. Specifically, we find that there is net magnetization in the flat nanoribbon along the Y-axis, which is perpendicular to the plane of the nanoribbon. However, when we bend the nanoribbon along its width direction (X axis), we observe a net magnetization along both the X axis and Y axis. This suggests that bending can have a significant impact and controlling power on the magnetic properties of defective A13WS$_2$ nanoribbons. The results for r^{2}SCAN and mTASK functionals are also consistent with the results obtained using PBE functional (see Supplemental Table SI and Table SII) [78].

For the pristine A13WS$_2$ nanoribbons, the site resolved SOC energy on each W atom shows a similar pattern as it was found by Tang *et al.* [55], as shown in Supplemental Fig. S3 [78]. The detailed analysis for the site resolved SOC energy on each W atom for defective A13WS$_2$ nanoribbons is presented in the Supplemental Material [78].

Next, we analyze the fundamental band gaps and defect levels with semilocal density functional approximations, and compare the energy levels to the ones of higher-level hybrid functional HSE06 and one-shot GW. We present the band gaps between VBM and CBM for the pristine A13WS$_2$ nanoribbons with various bending radii and with central S vacancy in Table I.

Metageneralized gradient approximations (meta-GGAs) of the third-rung of Jacob's ladder [79] such as SCAN, r^{2}SCAN in the generalized Kohn-Sham approximation [80,81] are

TABLE II. Calculated magnetization (in unit Bohr magneton μ_B per supercell) for bent and defective A13WS$_2$ nanoribbons with the PBE approximation.

Defect	Flat			R12			R7		
	X axis	Y axis	Z axis	X axis	Y axis	Z axis	X axis	Y axis	Z axis
None	0	0	0	−0.004	0	0	−0.004	0	0
S	−0.007	0	0	−0.003	0	0	0	0	0
W	0	0.275	0	−0.022	0.116	0.002	−0.064	0.106	0

known to slightly open band gaps compared to PBE-GGA [82,83]. The r^{2}SCAN results in larger band gaps in A13WS$_2$ nanoribbons than PBE. While we noted that r^{2}SCAN resulted in larger band gaps than PBE, it is essential to acknowledge that there is a broader range of DFT methods available for such band gap predictions. Recent research, including the work by Tran *et al.* [84], has demonstrated that alternative DFAs, such as GLLB-SC (GLLB abbreviates for author names and SC stands for solid and correlation), and the modified Becke-Johnson (mBJ), can also offer improved accuracy in predicting band gaps for low-dimensional materials when compared to PBE. These methods have been particularly successful in capturing the electronic structure of materials with reduced dimensionality. The TASK and mTASK meta-GGA's achieve even more nonlocality at the price of losing accuracy for ground state properties [58,85]. Within this work we focus on mTASK that proved a more suitable choice for the fundamental band gaps of materials with low dimension. The mTASK improves the band gaps in comparison to both PBE and r^{2}SCAN, capturing 55–59% of the GW value for the flat pristine and S-defective nanoribbon. The accuracy decreases with bending, specifically when the S vacancy is present, and the decrease in accuracy is more conspicious with mTASK than with r^{2}SCAN. r^{2}SCAN also makes the band gaps correctly direct as HSE06 and GW do. mTASK, although improves band gaps in general, but band dispersion was found unreliable [85]. The GW method with the nonlocal self-energy correction produces significantly larger band gaps than density functional approximations, highlighting the importance of the nonlocal self-energy in these quasi-one-dimensional materials.

The computationally more feasible semilocal DFT is useful to establish the trend between in-gap edge, and defect states in bent and defected A13WS$_2$ nanoribbons, as shown in Table III and Fig. 5. Our results reveal that the NEG band gap remains almost the same for the flat and bent (R = 12 Å) nanoribbons using PBE, while it slightly increases using r^{2}SCAN, mTASK and HSE06. This result emphasizes the predictive power of r^{2}SCAN, mTASK and HSE06 compared to PBE in simulations of more localized defect states. However, increasing the bending curvature leads to a decrease in the NEG band gap using PBE, r^{2}SCAN, mTASk, and HSE06 density functionals. Using the GW method, we observe a more enhanced decrease in the NEG band gap with increasing bending curvature. Edge and defect states are more localized than bulklike band states. Despite that they are localized states, density functional approximations display a different trend in accuracy. While there is no remarkable discrepancy between the accuracy of semilocal density functional approximations and HSE06 or GW for defect band gaps, the accuracy of the edge states varies more significantly from switching from PBE to meta-GGA and nonlocal approximations.

B. Optical absorption and exciton states

1. A13WS$_2$ *nanoribbon without defects*

Figures 6(a)–6(h) represent different physical parameters of the band structures for the flat and bent (with bending curvature radius R = 7 Å) A13WS$_2$ nanoribbon without defects. In the case of the flat nanoribbon, the site-resolved DOS plot (b) shows that the relatively separated eight bands around the Fermi level mainly arise from the edge W atoms (blue dots). Among the eight bands, there are four conduction bands forming the upper edge bands and four valence bands forming the lower edge bands. The spin-polarization of those edge bands calculated from PBE (c) and G_0W_0 (d) are similar, although G_0W_0 produces a much larger band gap (1.82 eV) than that (0.47 eV) of PBE, as a manifestation of the significant self-energy correction from the many-body effects. In the bent nanoribbon at R = 7 Å, the four lower edge bands are merged

TABLE III. Comparison of NEG, EG, and DG for PBE, r^{2}SCAN, and mTASK density functionals with the higher-level hybrid functional HSE06 or with the G0W0 approximation within many-body perturbation theory for bent and defective A13WS$_2$ nanoribbons. The fundamental band gaps are in eV.

	Defect	PBE			r^{2}SCAN			mTASK			HSE06			GW		
		NEG	EG	DG	NEG	EG	DG	NEG	EG	DG	NEG	EG	DG	NEG	EG	DG
Flat	None	1.90	0.48	N/A	2.02	0.73	N/A	2.18	1.00	N/A	2.60	1.25	N/A	3.43	1.82	N/A
	S	1.97	0.50	0.21	2.05	0.75	0.24	2.26	1.08	0.18	2.61	1.27	0.20	3.52	1.83	0.23
R12	None	1.92	0.42	N/A	2.10	0.67	N/A	2.33	0.84	N/A	2.70	1.13	N/A	3.37	1.80	N/A
	S	1.98	0.54	0.63	2.14	0.79	0.64	2.36	0.96	0.58	2.78	1.28	0.68	3.47	1.95	0.67
R7	None	1.21	0.38	N/A	1.33	0.54	N/A	1.47	0.77	N/A	1.81	1.00	N/A	2.59	1.67	N/A
	S	1.60	0.46	0.77	1.73	0.53	0.57	1.87	0.54	0.48	2.33	0.99	0.63	3.07	1.66	0.74

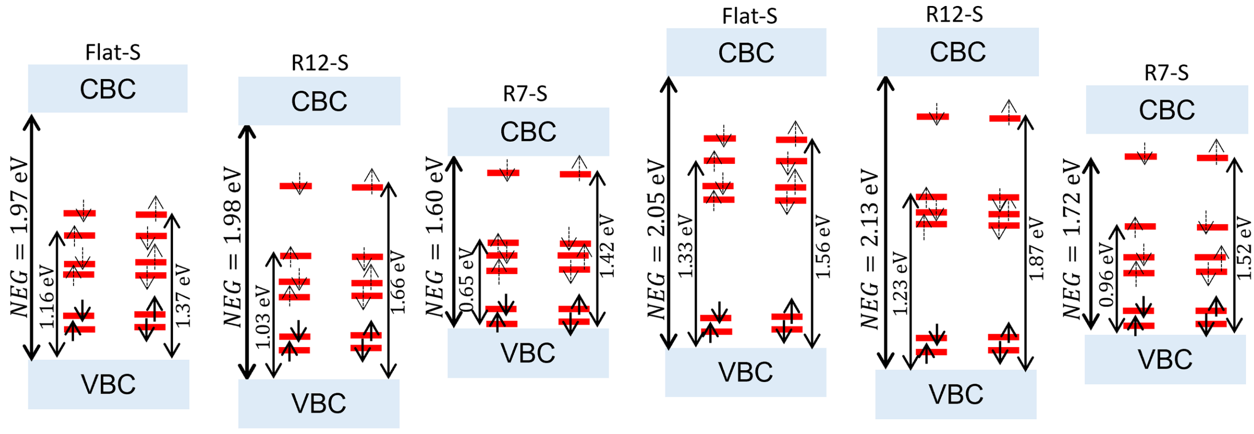

(a) PBE (b) r^2SCAN

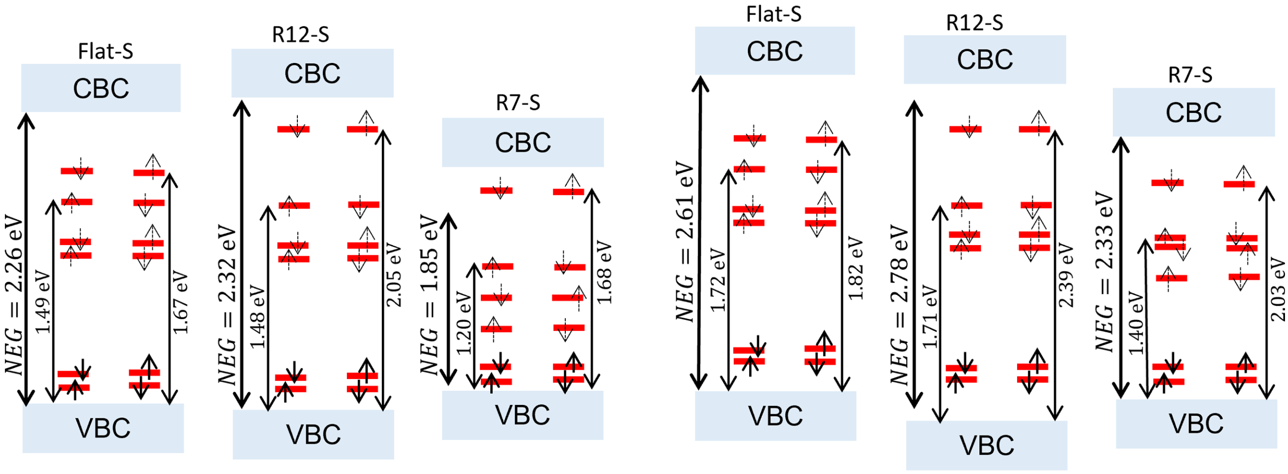

(c) mTASK (d) HSE06

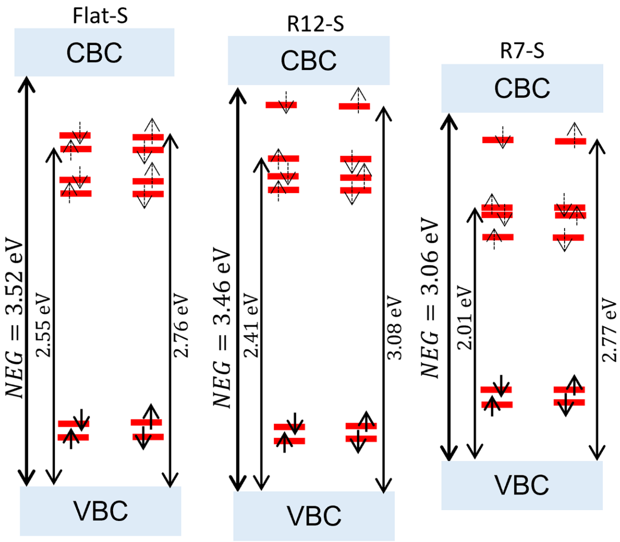

(e) GW

FIG. 5. Schematic diagram for quasiparticle energies of edge states and defect states at the Γ point of A13WS$_2$ using PBE, r^{2}SCAN and mTASK density functionals, the higher-level hybrid functional HSE06, and the GW method. The bottom four levels correspond to the lower edge bands occupied with electrons with spin up or down, while the other remaining levels correspond to the unoccupied upper edge bands and defect bands with spin up or down.

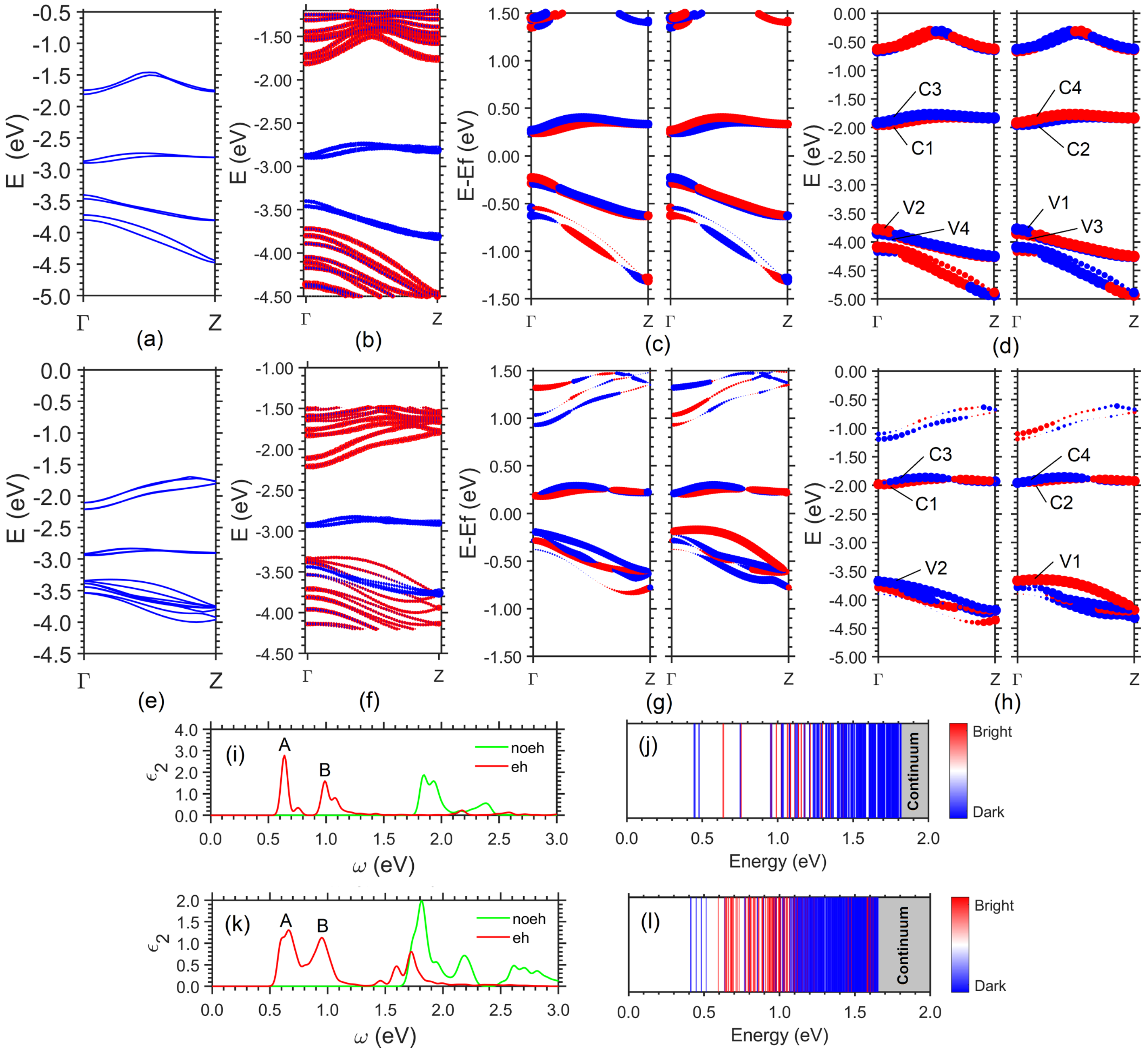

FIG. 6. The various band structures of the pristine A13WS$_2$ nanoribbon and its optical absorption and exciton spectra. Panels (a), (b), (c), and (d) are the PBE+SOC band structure, the site-DOS-resolved band structure, the PBE+SOC spin-polarization-resolved band structure, and the G_0W_0 spin-polarization-resolved band structure for the flat nanoribbon, respectively. (e), (f), (g), and (h) are the similarly organized band structures for the bent nanoribbon at R = 7 Å. The blue dots in (b) and (f) represent the contribution by edge W atoms, while red ones by other atoms in the nanoribbon. In (c), (d), (g), and (h), the odd number indexed bands are shown on the left subpanel and the even number indexed ones on the right subpanel for clarity, and the spin-up and spin-down polarizations are represented by red dots and blue dots, respectively. Band labels V1, V2, ... and C1, C2, ... are the other way to count the bands away from the Fermi level. (i) and (j) show the optical absorption and exciton spectra, respectively, for the flat nanoribbon without defects. The former is plotted as the imaginary part of the dielectric function as a function of photon energy with the red curve representing the GW+BSE result with electron-hole (eh) interactions and the green one for that without eh (noeh) interactions, both with constant broadening of 28 meV. (k) and (l) are similarly plotted and arranged for the bent (with R = 7 Å) nanoribbon without defects. Bright (dark) exciton states are represented by red (blue) lines in (j) and (l).

into the valence band continuum, as shown in the DOS plot (f). The PBE band gap of the bent nanoribbon is reduced to 0.35 eV from the 0.47 eV of the flat nanoribbon, and the G_0W_0 gap of the bent nanoribbon is reduced to 1.67 eV from the 1.82 eV of the flat one.

This rich interplay of bending and screening contributes to the optical response of nanoribbons, that reflects the alteration of screening with increased bending. Figures 6(i)–6(l) show the calculated optical absorption and exciton spectra for the flat and bent nanoribbons, showing strong excitonic effects. For the flat nanoribbon, the absorption mainly peaks around 0.65 and 1.00 eV. The bent nanoribbon shows two broad absorption peaks, which slightly extend to the low energy direction by about 0.05 eV, compared with those of the flat

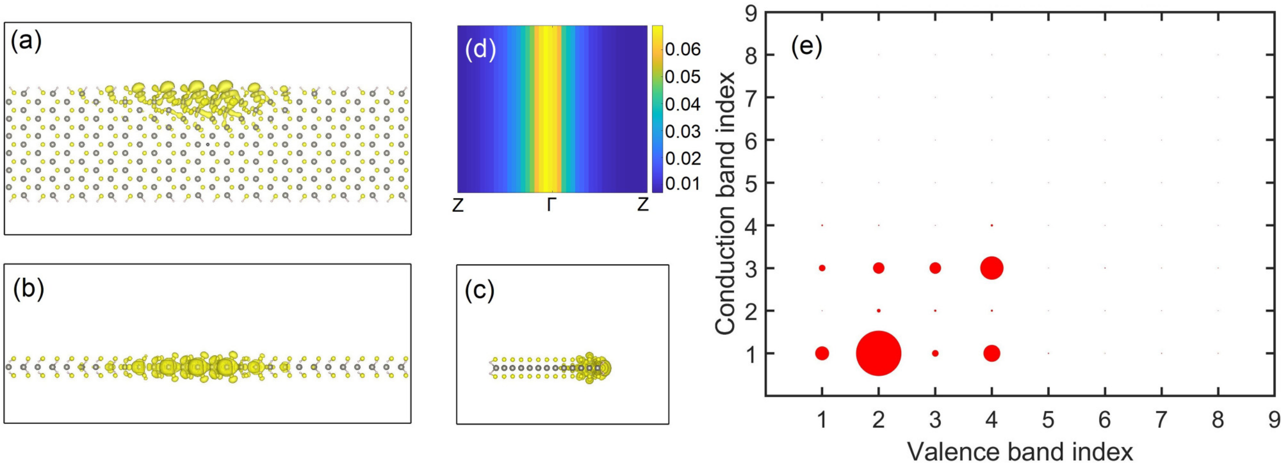

FIG. 7. The dark exciton at 0.44 eV of the pristine flat A13WS$_2$ nanoribbon. (a), (b), and (c) represent the three views of the isosurface contour of the modulus squared of the exciton wave function in real space, where the hole [black spot in (a)] is located at the center of the ribbon and near a W atom. The profile of the modulus squared exciton wave function in k space is shown in (d). (e) shows the contributing hole (valence) and electron (conduction) bands for each exciton. The valence (conduction) band index is counted downwards (upwards) from the Fermi level. The spot size in (e) is proportional to $\sum_k |A_{v,c}(k)|^2$ and represents the contributing weight from the v-c pair.

case, due to the slightly decreased fundamental band gap. A few small peaks are detected in the bent nanoribbon at around 1.5 to 1.8 eV, which are not present in the flat nanoribbon. Bending induces more bright exciton states within the range of 0.5–1.0 eV.

Both the flat and bent nanoribbons show several dark exciton states, and the lowest exciton state is a dark exciton, with mainly transitions from the lower edge to the upper edge bands [as shown in Fig. 7(e)]. The dark exciton at 0.45 eV exhibits similar physics (Supplemental Fig. S5) [78]. The bright excitons makes peak A at 0.64 eV in the flat nanoribbon [Fig. 6(i)], and its spatial extension is shown in the Supplemental Figs. S6 and S7 [78]. Another bright exciton with high oscillator strength appears at peak B at 0.99 eV (See Supplemental Fig. S8) [78].

In the bent nanoribbon with R = 7 Å, the dark excitons are shifted to 0.41 eV and 0.48, and they become localized at the edge (See Supplemental Figs. S9 and S10) [78]. Bright excitons shift similarly by bending, peak A to 0.63 eV, and peak B to 0.95 eV, mostly preserving the nature of their transition states, (See Supplemetal Figs. S11 and S12) [78].

2. A13WS$_2$ *nanoribbon with a line of S vacancy defects*

We also calculated the optical absorption and exciton states for the A13WS$_2$ nanoribbon with a line of sulfur vacancy defects. In the flat defective nanoribbon, the relaxed structure almost remains flat and only slightly deformed around the middle of the ribbon. The PBE band structure and the DOS resolved band structure are shown in Figs. 8(a) and 8(b), respectively. The four upper edge and the four lower edge bands remain around the Fermi level. The defect-derived four conduction bands are located higher than the upper edge bands. The defect-derived valence bands are mixed with bulk bands in the valence band continuum (VBC), while the top of VBC is mainly bulk atom derived. The fundamental band gap is 0.49 eV from PBE and 1.83 eV from G_0W_0.

For the same defective A13WS$_2$ nanoribbon under bending at R = 7 Å, the PBE band structure and the DOS resolved band structure are shown in Figs. 8(e) and 8(f), respectively. The conduction bands C1 and C2 are almost degenerate in energy. The DOS of C1 and C2 shows a mixture of edge (blue spots) and defect states (green spots) in Fig. 8(f), while the valence band V1 mainly consists of the bulk states (red spots) of the nanoribbon. The spin-polarization resolved band structures of the same bent nanoribbon calculated from both PBE and G_0W_0 methods [Figs. 8(g) and 8(h)], indicate that C1 is spin-up, while C2 is spin-down polarized within PBE (the r^{2}SCAN and mTASK functionals also show the similar spin states for C1 and C2, see Supplemental Figs. S27 and S28, respectively) [78], while the polarization is switched in G_0W_0. The fundamental gap increases from 0.45 eV in PBE to 1.66 eV in G_0W_0.

The optical absorption and exciton spectra are shown in Figs. 8(i) and 8(j), respectively for the flat and defective nanoribbon and in Figs. 8(k) and 8(l) for the bent defective nanoribbon with R = 7 Å. The optical absorption of the defective nanoribbon [Fig. 8(i)] remains similar to that of the pristine nanoribbon [Fig. 6(i)], especially regarding the positions of peaks A and B and the overall shapes of the peaks, as indicators that line defects behave similarly as edge state, and they do not significantly alter the optical response. Since the S vacancy line almost has no coupling with the edge bands of the flat ribbon, the positions of the upper and lower edge bands in the G_0W_0 band structures do not differ in the pristine and defective flat nanoribbon, leaving the optical absorption spectra with only some minor changes with excitonic peaks around 1.5 eV in the defective nanoribbon.

In the flat defective nanoribbon, the exciton states with the lowest energy at 0.46 and 0.47 eV is still a dark exciton, (See Supplemental Figs. S13, S14) [78]. There are two bright excitons with almost degenerate energy at 0.65 eV, and with mixed spin configurations (See Supplemental Figs. S15 and S16) [78]. Peak B consists of several bright excitons and there are two energy-degenerate ones at 0.997 eV. The wave functions

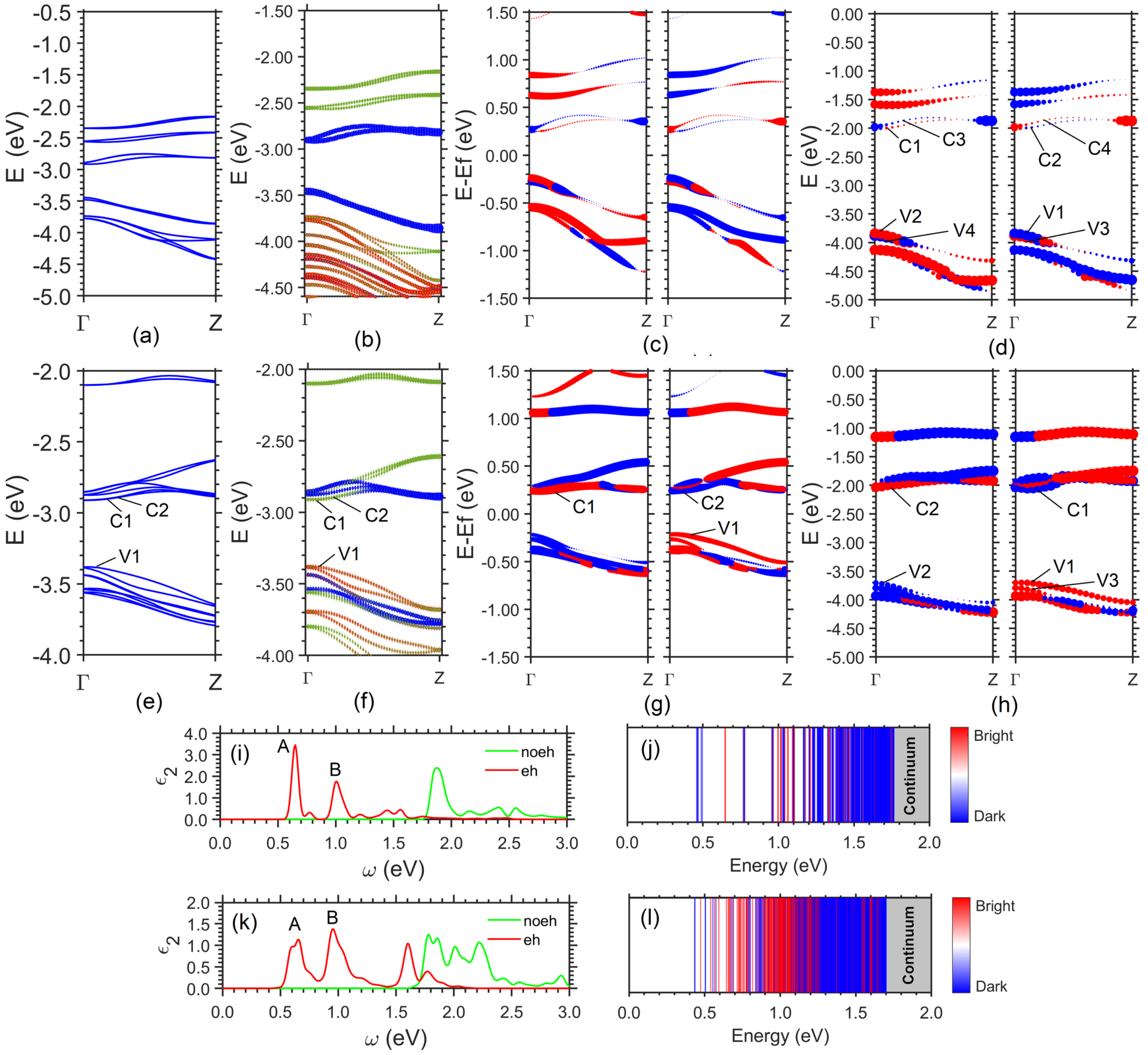

FIG. 8. The various band structures of the defective A13WS$_2$ nanoribbon with a sulfur defect line, and its optical absorption and exciton spectra. [(a)–(l)] are similarly obtained and arranged as in Fig. 6, with [(a)–(d)], [(i) and (j)] for the defected flat nanoribbon and panels [(e)–(h)], (k) and (l) for the defective bent nanoribbon with R = 7 Å. The blue dots in (b) and (f) are contributed by edge W atoms, the green ones from the atoms near the defect, and the red ones from other bulk atoms in the nanoribbon.

of the two bright excitons show slightly nodal features both in the real space and momentum space and they occupy different edge (See Supplemental Figs. S17 and S18) [78]. There is also a bright exciton at 1.01 eV. The valence bands V1-V8 have major contributions from the edge and bulk atoms and a minor contribution from the defect, (See Supplemental Fig. S19) [78].

In the bent defective nanoribbon, the optical absorption spectrum shows a similar shape and peak positions with those of the pristine nanoribbon with the same bending curvature radius R = 7 Å, especially within the energy range of 0.5–1.0 eV. Similar to the pristine bent nanoribbon, the lower four edge bands merge into the valence band continuum under bending, and the V1 and V2 are bulk derived. The four upper edge bands are mixed to some extent with the two lower defect-derived conduction bands. These common features make the optical absorption spectra of the pristine and defective bent nanoribbons share similar shapes within 0.5–1.0 eV.

Due to the mixture of the upper edge bands and the defect derived conduction bands, the exciton states formed in the defective bent nanoribbon show some different features. The exciton with the lowest energy at 0.43 eV is a dark exciton, which is due to the transitions from V1-V8 (including the bulk and lower edge bands) to C1-C6 (including the four upper edge bands and two defect derived conduction bands). The

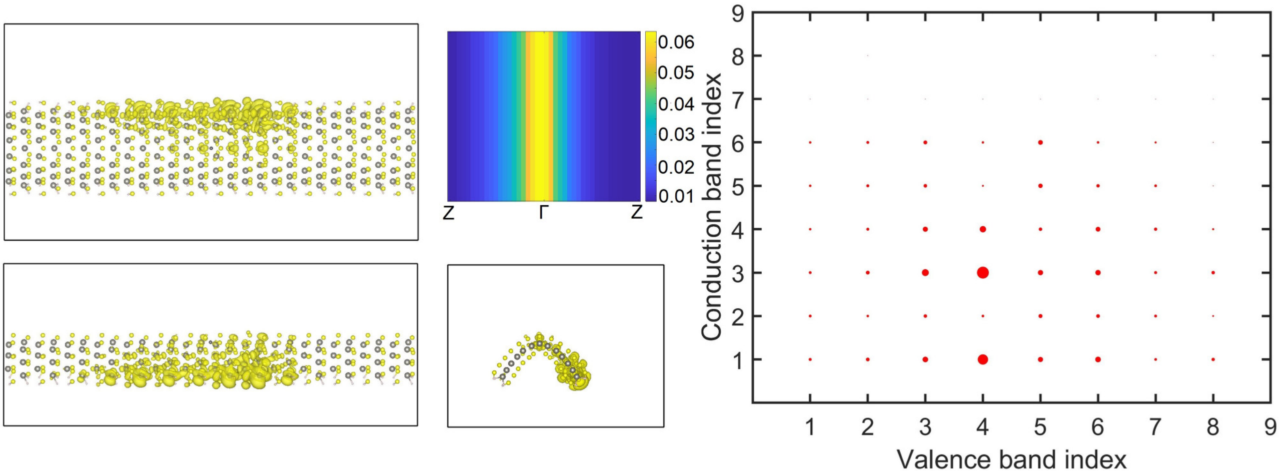

FIG. 9. The dark exciton at 0.43 eV of the defected bent (R = 7 Å) A13WS2 nanoribbon with a line of sulfur vacancy defects. Panels are plotted and arranged in the same way as in Fig. 7.

wave function of this exciton in real space is mainly located on one of the edges and also extended slightly along the central defect S line, confirming the relevant transitions to defect derived conduction bands, as shown in Fig. 9 (also see supplemental Fig. S20) [78]. The dark exciton at 0.51 eV is very similar to the one at 0.43 eV, and it is located on another edge and extended along the central defect S line (see Supplemental Fig. S21) [78]. Peak A consists of several bright excitons. The one at 0.57 eV is mainly due to the transition from V1 to C2 around Γ. Since V1 and C2 are both up-spin polarized, this bright exciton is mainly of like-spin configuration. Also, because of the admixing of edge and defect contributions in V1, the wave function of this exciton is largely extended along the central defect S line (see Supplemental Fig. S22) [78]. The wave functions of the two bright excitons at 0.64 and 0.66 eV also show the similar spatial extension along the central defect line (see supplemental Figures S23 and S24) [78], since their transitioned bands have defect derived features. The two excitons involve more band transitions and have a mixed spin configuration. The excitons in peak B show spatially more extended and nodal features, as can be seen from those of excitons at 0.93 and 0.95 eV (see Supplemental Figs. S25 and S26) [78], which are related to transitions from V1–V8 to C1–C6. Generally, they have a rich and mixed spin configuration.

The optical absorption shows a robust feature against the central sulfur defect line, while the exciton's extension can be controlled across the nanoribbon with appropriately applied bending. This may provide a fine-tuning knob for the exciton dynamics in the nanoribbons through the defect line and bending engineering. For example, one can switch the exciton between the edge and the center of the nanoribbon by bending, and selectively switch the interaction of excitons with other attached species. The existence of metallic excitons was reported and discussed several times. Such metallic excitons result from an imperfect screening of the electron-hole interaction in metals and are related to the so-called ghost plasmon [86–89] and in the recent work by Koskelo *et al.* [90]. The BSE calculations for metallic states in the current code (BerkeleyGW) we used are not available and the GW calculations for metallic states are computationally demanding, indicating more interesting future studies in this direction.

Unlike the optical absorption spectra, exciton lifetimes are strongly impacted by line defects and bending. We calculated the intrinsic exciton lifetimes for the pristine and defective A13WS$_2$ nanoribbons under various bending curvatures, and the results are presented in Fig. 10. Typically, low-energy dark excitons have intrinsic lifetimes ranging from 0.1 to around 300 μs, much smaller than those observed in monolayer WS$_2$ which is 3.7 ms [91]. The further reduced dimensionality of the quasi-1D nanoribbon system increases electron-electron interactions and the strength of the exciton transition dipole, and hence reduces the intrinsic lifetime. The flat and nondefective nanoribbon has a larger lifetime ($\sim$300 μs) for the lower energy dark excitons in comparison to the flat and defective nanoribbon which has the lifetime of $\sim$2 μs, consistent with the usual experimental results of faster recombination of excitons in defected monolayer systems [92]. For the bent nanoribbons with or without defects, the intrinsic lifetimes (~ 0.1 μs) for the low energy dark excitons are further reduced. This may be due to the merging of the lower edge states into valence band continuum at large bending, which results in a large mixing of edge and bulk states for the hole wave function, increasing the overlapping of wave functions of the electron and hole in the excitons, hence increasing the recombination rate of electron and hole and decreasing the lifetime of excitons. Our results show that bending and defects can manifestly modify and control the lifetimes of excitons in the WS$_2$ nanoribbons. These relatively large lifetimes ($\sim 0.1 - 300$ μs) and tunability are instrumental in realizing exciton-based quantum controls and probing exciton dynamics. Since the nanoribbon has two edges and some excitons are apparently localized on the two edges, (see Supplemental Fig. S5-S8) [78] it is hard to estimate the size of those excitons. However, from the wave-function distributions of the excitons, we can estimate that the size of the exciton is roughly about 1–2 nm, approximately close to that in the monolayer TMD [93].

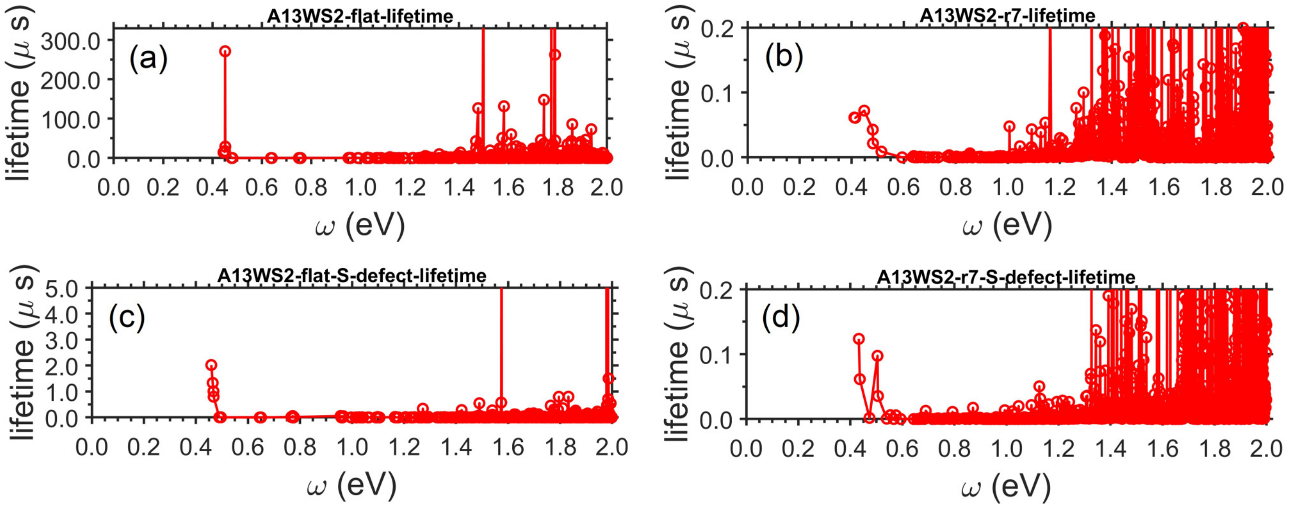

FIG. 10. The calculated exciton intrinsic lifetimes of the A13WS$_2$ nanoribbons. (a) for flat A13WS$_2$ without defects, (b) for bent (with R = 7 Å) A13WS$_2$ without defects, (c) for the flat and S defective A13WS$_2$, and (d) for the bent (with R = 7 Å) and S defective A13WS$_2$.

IV. CONCLUSIONS

In conclusion, we calculated the band structures and band gaps of armchair WS$_2$ nanoribbons with and without defects under various bending curvatures using density functional approximations (DFA), the screened-hybrid HSE06 approximation, and the quasiparticle GW method. We also investigated the optical absorption and excitonic states of these nanoribbons using the many body GW-BSE approximation.

The calculations reveal that the d orbitals of the edge W atoms are the primary source of both the upper edge bands and lower edge bands around the Fermi level. The defect bands are mainly derived from the d orbitals of the nearby defect W atoms in the nanoribbons. The phase of the nanoribbon can be controlled by the interplay of the defect location and bending in the nanoribbon. The A13WS$_2$ nanoribbon with a central lower S defect line remains semiconducting with increasing bending, where the upper defect bands move downward and eventually mix with the upper edge bands at a large bending curvature. The A13WS$_2$ nanoribbon with a central W defect line is metallic under all bending curvatures considered, while the A13WS$_2$ nanoribbon with a noncentral W defect line can exhibit a metal-to-semiconductor or semiconductor-to-metal phase transition with an appropriate bending curvature. Additionally, the A13WS$_2$ nanoribbon with a W defect line is magnetic, and the magnetization shows slight spatial variation with bending. These results suggest that properly designed defected and bent WS$_2$ nanoribbons can be utilized in heterophase homojunctions to avoid Schottky contact in phase-change electrical devices, as well as in magnetic nano-electronics or molecular electronics.

The band gaps calculated using the mTASK functional are generally larger than those from PBE and r^{2}SCAN and are close to the values obtained from the screened-hybrid HSE06 functional, as a result of the more enhanced nonlocality in the exchange potential from the kinetic energy density ingredient. The GW method yields larger values of band gaps than all the tested methods indicating the large self-energy correction due to reduced screening in the quasi-one-dimensional nanoribbon system, but mTASK can be a reasonable alternative in high-throughput band gap calculations.

The calculated optical absorption spectra of flat WS$_2$ nanoribbons with and without a central sulfur defect line share a similar shape, emphasizing the dominance of edge-band transitions around the Fermi level. At a large bending curvature, the defect-derived upper conduction bands move downward and mix with the edge-derived bands, while the lower edge bands merge into the valence band continuum, making again the overall shape of the optical absorption spectra for the bent WS$_2$ nanoribbons with and without a central Sulphur defect line similar. However, the spatial distributions of the excitons of the defective bent nanoribbon are generally more in the central area of the nanoribbon, indicating the involvement of the defect-derived bands in the optical transitions. The defective A13WS$_2$ nanoribbon typically exhibits a rich and mixed spin configuration due to the mixing of upper edge bands and defect-derived conduction bands. Furthermore, the A13WS$_2$ nanoribbons show large calculated intrinsic lifetimes of dark excitons and a tunability in the intrinsic lifetime with bending, suggesting a useful application in exciton dynamics and exciton-based quantum technologies.

Overall, our work provides valuable insights into the electronic and optical properties of defected and bent WS$_2$ nanoribbons, offering prospects for their utilization in various technological fields.

ACKNOWLEDGMENTS

This material is based upon work supported by the U.S. Department of Energy (DOE), Office of Science, Office of Basic Energy Sciences, under Award No. DE-SC0021263. Computational support was provided by Temple University's HPC resources, resources of the National Energy Research Scientific Computing Center, a DOE Office of Science User

Facility supported by the Office of Science of the U.S. DOE under Contract No. DE-AC02-05CH11231.

We thank Prof. J. P. Perdew for his valuable comments on the manuscript.

---

[1] A. C. Ferrari, F. Bonaccorso, V. Fal'ko, K. S. Novoselov, S. Roche, P. Bøggild, S. Borini, F. H. L. Koppens, V. Palermo, N. Pugno, J. A. Garrido, R. Sordan, A. Bianco, L. Ballerini, M. Prato, E. Lidorikis, J. Kivioja, C. Marinelli, T. Ryhänen, A. Morpurgo, J. N. Coleman, V. Nicolosi, L. Colombo, A. Fert, M. Garcia-Hernandez, A. Bachtold, G. F. Schneider, F. Guinea, C. Dekker, M. Barbone, Z. Sun, C. Galiotis, A. N. Grigorenko, G. Konstantatos, A. Kis, M. Katsnelson, L. Vandersypen, A. Loiseau, V. Morandi, D. Neumaier, E. Treossi, V. Pellegrini, M. Polini, A. Tredicucci, G. M. Williams, B. Hee Hong, J.-H. Ahn, J. Min Kim, H. Zirath, B. J. van Wees, H. van der Zant, L. Occhipinti, A. Di Matteo, I. A. Kinloch, T. Seyller, E. Quesnel, X. Feng, K. Teo, N. Rupesinghe, P. Hakonen, S. R. T. Neil, Q. Tannock, T. Löfwander, and J. Kinaret, Nanoscale **7**, 4598 (2015).

[2] B. Radisavljevic, A. Radenovic, J. Brivio, V. Giacometti, and A. Kis, Nat. Nanotechnol. **6**, 147 (2011).

[3] J. N. Coleman, M. Lotya, A. O'Neill, S. D. Bergin, P. J. King, U. Khan, K. Young, A. Gaucher, S. De, R. J. Smith, I. V. Shvets, S. K. Arora, G. Stanton, H.-Y. Kim, K. Lee, G. T. Kim, G. S. Duesberg, T. Hallam, J. J. Boland, J. J. Wang, J. F. Donegan, J. C. Grunlan, G. Moriarty, A. Shmeliov, R. J. Nicholls, J. M. Perkins, E. M. Grieveson, K. Theuwissen, D. W. McComb, P. D. Nellist, and V. Nicolosi, Science **331**, 568 (2011).

[4] C. Ataca, H. Şahin, and S. Ciraci, J. Phys. Chem. C **116**, 8983 (2012).

[5] S. Lebègue, T. Björkman, M. Klintenberg, R. M. Nieminen, and O. Eriksson, Phys. Rev. X **3**, 031002 (2013).

[6] H. Terrones, F. López-Urías, and M. Terrones, Sci. Rep. **3**, 1549 (2013).

[7] F. A. Rasmussen and K. S. Thygesen, J. Phys. Chem. C **119**, 13169 (2015).

[8] K. S. Novoselov, A. K. Geim, S. V. Morozov, D. Jiang, Y. Zhang, S. V. Dubonos, I. V. Grigorieva, and A. A. Firsov, Science **306**, 666 (2004).

[9] M. I. Katsnelson, K. S. Novoselov, and A. K. Geim, Nat. Phys. **2**, 620 (2006),.

[10] K. S. Novoselov, D. Jiang, F. Schedin, T. J. Booth, V. V. Khotkevich, S. V. Morozov, and A. K. Geim, Proc. Natl. Acad. Sci. **102**, 10451 (2005).

[11] K. S. Novoselov, A. K. Geim, S. V. Morozov, D. Jiang, M. I. Katsnelson, I. V. Grigorieva, S. V. Dubonos, and A. A. Firsov, Nature (London) **438**, 197 (2005).

[12] Y. Zhang, Y.-W. Tan, H. L. Stormer, and P. Kim, Nature (London) **438**, 201 (2005).

[13] M. Chhowalla, H. S. Shin, G. Eda, L.-J. Li, K. P. Loh, and H. Zhang, Nat. Chem. **5**, 263 (2013).

[14] Q. H. Wang, K. Kalantar-Zadeh, A. Kis, J. N. Coleman, and M. S. Strano, Nat. Nanotechnol. **7**, 699 (2012).

[15] W. Lu and C. M. Lieber, Nat. Mater. **6**, 841 (2007).

[16] X. Qian, J. Liu, L. Fu, and J. Li, Science **346**, 1344 (2014).

[17] H. Fang, S. Chuang, T. C. Chang, K. Takei, T. Takahashi, and A. Javey, Nano Lett. **12**, 3788 (2012), pMID: 22697053.

[18] F. Schwierz, Nat. Nanotechnol. **5**, 487 (2010).

[19] J. D. Fowler, M. J. Allen, V. C. Tung, Y. Yang, R. B. Kaner, and B. H. Weiller, ACS Nano **3**, 301 (2009), pMID: 19236064,.

[20] K. Chang and W. Chen, ACS Nano **5**, 4720 (2011), pMID: 21574610,.

[21] R. Bhandavat, L. David, and G. Singh, J. Phys. Chem. Lett. **3**, 1523 (2012).

[22] A. R. Beal, H. P. Hughes, and W. Y. Liang, J. Phys. C **8**, 4236 (1975).

[23] S. Chandra, D. P. Singh, P. C. Srivastava, and S. N. Sahu, J. Phys. D **17**, 2125 (1984).

[24] T. Gokus, R. R. Nair, A. Bonetti, M. Böhmler, A. Lombardo, K. S. Novoselov, A. K. Geim, A. C. Ferrari, and A. Hartschuh, ACS Nano **3**, 3963 (2009).

[25] G. Eda, Y.-Y. Lin, C. Mattevi, H. Yamaguchi, H.-A. Chen, I.-S. Chen, C.-W. Chen, and M. Chhowalla, Adv. Mater. **22**, 505 (2010).

[26] M. N. Ali, J. Xiong, S. Flynn, J. Tao, Q. D. Gibson, L. M. Schoop, T. Liang, N. Haldolaarachchige, M. Hirschberger, N. P. Ong, and R. J. Cava, Nature (London) **514**, 205 (2014).

[27] K. F. Mak, K. He, J. Shan, and T. F. Heinz, Nat. Nanotechnol. **7**, 494 (2012).

[28] H. Zeng, J. Dai, W. Yao, D. Xiao, and X. Cui, Nat. Nanotechnol. **7**, 490 (2012).

[29] Z. Lin, A. McCreary, N. Briggs, S. Subramanian, K. Zhang, Y. Sun, X. Li, N. J. Borys, H. Yuan, S. K. Fullerton-Shirey, A. Chernikov, H. Zhao, S. McDonnell, A. M. Lindenberg, K. Xiao, B. J. LeRoy, M. Drndić, J. C. M. Hwang, J. Park, M. Chhowalla, R. E. Schaak, A. Javey, M. C. Hersam, J. Robinson, and M. Terrones, 2D Mater. **3**, 042001 (2016).

[30] Z. Wu and Z. Ni, Nanophotonics **6**, 1219 (2017).

[31] S. Wang, A. Robertson, and J. H. Warner, Chem. Soc. Rev. **47**, 6764 (2018).

[32] D. Rhodes, S. H. Chae, R. Ribeiro-Palau, and J. Hone, Nat. Mater. **18**, 541 (2019).

[33] P. K. Chow, R. B. Jacobs-Gedrim, J. Gao, T.-M. Lu, B. Yu, H. Terrones, and N. Koratkar, ACS Nano **9**, 1520 (2015).

[34] J. Hong, Z. Hu, M. Probert, K. Li, D. Lv, X. Yang, L. Gu, N. Mao, Q. Feng, L. Xie, J. Zhang, D. Wu, Z. Zhang, C. Jin, W. Ji, X. Zhang, J. Yuan, and Z. Zhang, Nat. Commun. **6**, 6293 (2015).

[35] Z. Wu, Z. Luo, Y. Shen, W. Zhao, W. Wang, H. Nan, X. Guo, L. Sun, X. Wang, Y. You, and Z. Ni, Nano Res. **9**, 3622 (2016).

[36] Y. Wan, E. Li, Z. Yu, J.-K. Huang, M.-Y. Li, A.-S. Chou, Y.-T. Lee, C.-J. Lee, H.-C. Hsu, Q. Zhan, A. Aljarb, J.-H. Fu, S.-P. Chiu, X. Wang, J.-J. Lin, Y.-P. Chiu, W.-H. Chang, H. Wang, Y. Shi, N. Lin, Y. Cheng, V. Tung, and L.-J. Li, Nat. Commun. **13**, 4149 (2022).

[37] X.-X. Zhang, T. Cao, Z. Lu, Y.-C. Lin, F. Zhang, Y. Wang, Z. Li, J. C. Hone, J. A. Robinson, D. Smirnov, S. G. Louie, and T. F. Heinz, Nat. Nanotechnol. **12**, 883 (2017).

[38] T. Li, S. Jiang, L. Li, Y. Zhang, K. Kang, J. Zhu, K. Watanabe, T. Taniguchi, D. Chowdhury, L. Fu, J. Shan, and K. F. Mak, Nature (London) **597**, 350 (2021).

[39] C. Jin, Z. Tao, T. Li, Y. Xu, Y. Tang, J. Zhu, S. Liu, K. Watanabe, T. Taniguchi, J. C. Hone, L. Fu, J. Shan, and K. F. Mak, Nat. Mater. **20**, 940 (2021).
[40] L. Ma, P. X. Nguyen, Z. Wang, Y. Zeng, K. Watanabe, T. Taniguchi, A. H. MacDonald, K. F. Mak, and J. Shan, Nature (London) **598**, 585 (2021).
[41] T. Li, S. Jiang, B. Shen, Y. Zhang, L. Li, Z. Tao, T. Devakul, K. Watanabe, T. Taniguchi, L. Fu, J. Shan, and K. F. Mak, Nature (London) **600**, 641 (2021).
[42] X. Hong, J. Kim, S.-F. Shi, Y. Zhang, C. Jin, Y. Sun, S. Tongay, J. Wu, Y. Zhang, and F. Wang, Nat. Nanotechnol. **9**, 682 (2014).
[43] N. Peimyoo, J. Shang, C. Cong, X. Shen, X. Wu, E. K. L. Yeow, and T. Yu, ACS Nano **7**, 10985 (2013).
[44] X. Duan, C. Wang, J. C. Shaw, R. Cheng, Y. Chen, H. Li, X. Wu, Y. Tang, Q. Zhang, A. Pan, J. Jiang, R. Yu, Y. Huang, and X. Duan, Nat. Nanotechnol. **9**, 1024 (2014).
[45] H. S. Lee, D. H. Luong, M. S. Kim, Y. Jin, H. Kim, S. Yun, and Y. H. Lee, Nat. Commun. **7**, 13663 (2016).
[46] S. Cho, S. Kim, J. H. Kim, J. Zhao, J. Seok, D. H. Keum, J. Baik, D.-H. Choe, K. J. Chang, K. Suenaga, S. W. Kim, Y. H. Lee, and H. Yang, Science **349**, 625 (2015).
[47] Z. Wang, X. Liu, J. Zhu, S. You, K. Bian, G. Zhang, J. Feng, and Y. Jiang, Sci. Bull. **64**, 1750 (2019).
[48] Y. Zhou, G. Scuri, D. S. Wild, A. A. High, A. Dibos, L. A. Jauregui, C. Shu, K. De Greve, K. Pistunova, A. Y. Joe, T. Taniguchi, K. Watanabe, P. Kim, M. D. Lukin, and H. Park, Nat. Nanotechnol. **12**, 856–860 (2017).
[49] C. Attaccalite, M. Bockstedte, A. Marini, A. Rubio, and L. Wirtz, Phys. Rev. B **83**, 144115 (2011).
[50] H. Wang, H. S. Wang, C. Ma, L. Chen, C. Jiang, C. Chen, X. Xie, A.-P. Li, and X. Wang, Nat. Rev. Phys. **3**, 791 (2021).
[51] G. Z. Magda, X. Jin, I. Hagymási, P. Vancsó, Z. Osváth, P. Nemes-Incze, C. Hwang, L. P. Biró, and L. Tapasztó, Nature (London) **514**, 608 (2014).
[52] H. Pan and Y.-W. Zhang, J. Mater. Chem. **22**, 7280 (2012).
[53] H. Tang, B. Neupane, S. Neupane, S. Ruan, N. K. Nepal, and A. Ruzsinszky, Sci. Rep. **12**, 3008 (2022).
[54] B. Neupane, H. Tang, N. K. Nepal, and A. Ruzsinszky, Phys. Rev. Mater. **6**, 014010 (2022).
[55] H. Tang, S. Neupane, L. Yin, J. M. Breslin, and A. Ruzsinszky, J. Mater. Chem. C **11**, 4711 (2023).
[56] J. P. Perdew, K. Burke, and M. Ernzerhof, Phys. Rev. Lett. **77**, 3865 (1996).
[57] J. W. Furness, A. D. Kaplan, J. Ning, J. P. Perdew, and J. Sun, J. Phys. Chem. Lett. **11**, 8208 (2020).
[58] B. Neupane, H. Tang, N. K. Nepal, S. Adhikari, and A. Ruzsinszky, Phys. Rev. Mater. **5**, 063803 (2021).
[59] J. Heyd, G. E. Scuseria, and M. Ernzerhof, J. Chem. Phys. **118**, 8207 (2003).
[60] L. Hedin, Phys. Rev. **139**, A796 (1965).
[61] L. Hedin and S. Lundqvist, “Effects of electron-electron and electron-phonon interactions on the one-electron states of solids,” in *Solid State Physics*, edited by F. Seitz, D. Turnbull, and H. Ehrenreich (Academic, New York,, 1969), Vol. 23, pp. 1–181.
[62] M. S. Hybertsen and S. G. Louie, Phys. Rev. Lett. **55**, 1418 (1985).
[63] F. Aryasetiawan and O. Gunnarsson, Rep. Prog. Phys. **61**, 237 (1998).
[64] P. Hohenberg and W. Kohn, Phys. Rev. **136**, B864 (1964).
[65] W. Kohn and L. J. Sham, Phys. Rev. **140**, A1133 (1965).
[66] G. Kresse and J. Furthmüller, Phys. Rev. B **54**, 11169 (1996).
[67] P. E. Blöchl, Phys. Rev. B **50**, 17953 (1994).
[68] G. Kresse and D. Joubert, Phys. Rev. B **59**, 1758 (1999).
[69] G. Onida, L. Reining, and A. Rubio, Rev. Mod. Phys. **74**, 601 (2002).
[70] S. Albrecht, L. Reining, R. Del Sole, and G. Onida, Phys. Rev. Lett. **80**, 4510 (1998).
[71] L. X. Benedict, E. L. Shirley, and R. B. Bohn, Phys. Rev. Lett. **80**, 4514 (1998).
[72] M. Rohlfing and S. G. Louie, Phys. Rev. Lett. **80**, 3320 (1998).
[73] W. Hanke and L. J. Sham, Phys. Rev. B **21**, 4656 (1980).
[74] J. Deslippe, G. Samsonidze, D. A. Strubbe, M. Jain, M. L. Cohen, and S. G. Louie, Comput. Phys. Commun. **183**, 1269 (2012).
[75] P. Giannozzi, S. Baroni, N. Bonini, M. Calandra, R. Car, C. Cavazzoni, D. Ceresoli, G. L. Chiarotti, M. Cococcioni, I. Dabo, A. D. Corso, S. de Gironcoli, S. Fabris, G. Fratesi, R. Gebauer, U. Gerstmann, C. Gougoussis, A. Kokalj, M. Lazzeri, L. Martin-Samos, N. Marzari, F. Mauri, R. Mazzarello, S. Paolini, A. Pasquarello, L. Paulatto, C. Sbraccia, S. Scandolo, G. Sclauzero, A. P. Seitsonen, A. Smogunov, P. Umari, and R. M. Wentzcovitch, J. Phys.: Condens. Matter **21**, 395502 (2009).
[76] C. D. Spataru, S. Ismail-Beigi, R. B. Capaz, and S. G. Louie, Phys. Rev. Lett. **95**, 247402 (2005).
[77] M. Re Fiorentin, F. Risplendi, M. Palummo, and G. Cicero, ACS Applied Nano Mater. **4**, 1985 (2021).
[78] See Supplemental Material at http://link.aps.org/supplemental/10.1103/PhysRevMaterials.7.124001 for additional information, including: the structures of nanoribbons with S and W vacancies defects (with atom indexes for W atoms), the structures of nanoribbons showing defect locations for the phase diagram, the calculated net magnetizations using r^{2}SCAN and mTASK functionals, a detailed description of the site-resolved SOC energy on each W atom for defective A13WS$_2$ nanoribbons, the dark and bright excitons of both flat and bent nanoribbons with and without defects, and a comparison of band structures of the nanoribbons using r^{2}SCAN and mTASK functionals with GW method, etc.
[79] J. P. Perdew and K. Schmidt, in Density Functional Theory and its Application to Materials, AIP Conf. Proc. **577**, 1 (2001).
[80] Z. H. Yang, H. Peng, J. Sun, and J. P. Perdew, Phys. Rev. B **93**, 205205 (2016).
[81] A. Seidl, A. Görling, P. Vogl, J. A. Majewski, and M. Levy, Phys. Rev. B **53**, 3764 (1996).
[82] J. P. Perdew, W. Yang, K. Burke, Z. Yang, E. K. U. Gross, M. Scheffler, G. E. Scuseria, T. M. Henderson, I. Y. Zhang, A. Ruzsinszky, H. Peng, J. Sun, E. Trushin, and A. Görling, Proc. Natl. Acad. Sci. **114**, 2801 (2017).
[83] M. Kothakonda, A. D. Kaplan, E. B. Isaacs, C. J. Bartel, J. W. Furness, J. Ning, C. Wolverton, J. P. Perdew, and J. Sun, ACS Materials Au **3**, 102 (2023).
[84] F. Tran, J. Doumont, L. Kalantari, P. Blaha, T. Rauch, P. Borlido, S. Botti, M. A. L. Marques, A. Patra, S. Jana, and P. Samal, J. Chem. Phys. **155**, 104103 (2021).
[85] T. Aschebrock and S. Kümmel, Phys. Rev. Res. **1**, 033082 (2019).
[86] A. Marini and R. Del Sole, Phys. Rev. Lett. **91**, 176402 (2003).

[87] A.-M. Uimonen, G. Stefanucci, Y. Pavlyukh, and R. van Leeuwen, Phys. Rev. B **91**, 115104 (2015).
[88] J. Deslippe, C. D. Spataru, D. Prendergast, and S. G. Louie, Nano Lett. **7**, 1626 (2007).
[89] Y. Liang, R. Soklaski, S. Huang, M. W. Graham, R. Havener, J. Park, and L. Yang, Phys. Rev. B **90**, 115418 (2014).
[90] J. Koskelo, L. Reining, and M. Gatti, arXiv:2301.00474.
[91] M. Palummo, M. Bernardi, and J. C. Grossman, Nano Lett. **15**, 2794 (2015).
[92] H. Shi, R. Yan, S. Bertolazzi, J. Brivio, B. Gao, A. Kis, D. Jena, H. G. Xing, and L. Huang, ACS Nano **7**, 1072 (2013).
[93] D. Y. Qiu, F. H. da Jornada, and S. G. Louie, Phys. Rev. Lett. **111**, 216805 (2013).